

Molecular modeling of interfacial properties
of the hydrogen+water+decane mixture
in three-phase equilibrium

Yafan Yang^{1,†}, Jingyu Wan^{2,†}, Jingfa Li[‡],
Guangsi Zhao[†], and Xiangyu Shang^{3,†}

[†] State Key Laboratory for Geomechanics and Deep
Underground Engineering, China University of Mining
and Technology, Xuzhou 221116, China.

[‡] School of Mechanical Engineering and Hydrogen
Energy Research Center, Beijing Institute of
Petrochemical Technology, Beijing 102617, China.

July 31, 2023

¹Corresponding Author, email address: yafan.yang@cumt.edu.cn

²Corresponding Author, email address: jingyu_wan123@163.com

³Corresponding Author, email address: xyshang@cumt.edu.cn

Abstract

The understanding of geochemical interactions between H_2 and geofluids is of great importance for underground H_2 storage, but requires further study. We report the first investigation on the three-phase fluid mixture containing H_2 , H_2O , and $\text{n-C}_{10}\text{H}_{22}$. Molecular dynamics simulation and PC-SAFT density gradient theory are employed to estimate the interfacial properties under various conditions (temperature ranges from 298 to 373 K and pressure is up to around 100 MPa). Our results demonstrate that interfacial tensions (IFTs) of the H_2 - H_2O interface in the $\text{H}_2+\text{H}_2\text{O}+\text{C}_{10}\text{H}_{22}$ three-phase mixture are smaller than IFTs in the $\text{H}_2+\text{H}_2\text{O}$ two-phase mixture. This decrement of IFT can be attributed to $\text{C}_{10}\text{H}_{22}$ adsorption in the interface. Importantly, H_2 accumulates in the H_2O - $\text{C}_{10}\text{H}_{22}$ interface in the three-phase systems, which leads to weaker increments of IFT with increasing pressure compared to IFTs in the water+ $\text{C}_{10}\text{H}_{22}$ two-phase mixture. In addition, the IFTs of the H_2 - $\text{C}_{10}\text{H}_{22}$ interface are hardly influenced by H_2O due to the limited amount of H_2O dissolved in bulk phases. Nevertheless, relatively strong enrichments and positive surface excesses of H_2O are seen in the H_2 - $\text{C}_{10}\text{H}_{22}$ interfacial region. Furthermore, the values of the spreading coefficient are mostly negative revealing the presence of the three-phase contact for the $\text{H}_2+\text{H}_2\text{O}+\text{C}_{10}\text{H}_{22}$ mixture under studied conditions.

KEYWORDS: Three phase mixture; Interfacial tension; Square gradient theory; PC-SAFT; Molecular simulation; Underground H_2 storage.

1 Introduction

The discharge of greenhouse gases into the air through the burning of fossil fuels is a major environmental issue since it contributes to global warming.^{1,2} The progressive substitution of fossil fuels with hydrogen as a clean fuel has garnered significant attention. Utilizing renewable resources for hydrogen production has the potential to significantly decrease carbon emissions, thereby playing an important role in mitigating climate change.³⁻⁵

A significant challenge lies in the limited hydrogen storage capacity in times of excess production.⁶⁻⁸ Over the years, there has been successful implementation of industrial-scale storage of natural gas in geological locations, such as in depleted gas/oil reservoirs (80%), saline aquifers (12%), and salt caverns (8%).⁹ Nonetheless, when it comes to storing pure H₂ at an industrial scale, only salt caverns have been employed so far.¹⁰ There have been limited instances where other sites like aquifers and depleted gas reservoirs have been used effectively to store gas mixtures containing H₂.^{11,12} Therefore, exploring alternative storage site options holds immense importance and warrants further investigation.

Depleted oil reservoirs have proven successful in storing natural gas and CO₂,^{9,13} but they have not been utilized for H₂ storage. Unlike CH₄ and CO₂, H₂ exhibits large minimum miscibility pressures with oil.¹⁴⁻¹⁶ Consequently, the geological storage of H₂ in depleted oil fields is mostly expected to encounter a three-phase fluid system. The interfacial characteristics of multiphase fluid systems play a critical role in determining the capillary entry pressure required for gas penetration in the pores.^{17,18} This, in turn, significantly affects the efficiency of the capillary sealing of the caprocks in depleted oil reservoirs, making it one of the key influencing parameters.^{17,19,20}

Recently, many investigations, both experimental²¹⁻²⁸ and simulation-based,²⁹⁻³¹ have been conducted to examine the interfacial characteristics in two-phase mixtures that involve both hydrogen and water. The interfacial tension (IFT) of the hydrogen+water mixture exhibits a nearly linear reduction in response to increments of

pressure and temperature, and at elevated temperatures, the decrease in IFT from rising pressure is less pronounced.^{21–25} The IFTs of H₂+brine systems show a proportional increase as the salinity rises.^{23,26} Moreover, the inclusion of impurities such as N₂, CO₂, and/or CH₄ in the gas+H₂+H₂O two-phase systems leads to decrements in IFTs.^{21,26–28} In addition, molecular dynamics (MD) simulations predict IFTs in the hydrogen+water system with reasonable accuracy comparing experimental data.^{29–31} Importantly, adsorption of hydrogen in the interfacial region of the hydrogen+water mixture has been observed based on the density distributions from MD simulations, which explains the relatively small IFT in contrast to the surface tension of pure H₂O.³⁰

Meanwhile, several studies have focused on the characteristics of interfaces in the gas+H₂O+oil three-phase mixtures.^{32–41} Three different interfaces are involved in the gas+H₂O+oil three-phase mixtures, namely, the gas-H₂O, the gas-oil, and the H₂O-oil interfaces. Generally, the IFTs of the CH₄-H₂O interface in three-phase systems containing CH₄/CO₂+H₂O+oil^{30,38} are lower than those in two-phase systems of H₂O+gas.⁴² This observation from MD simulations can be attributed to the presence of an excess of oil in the interface. The presence of gases (CH₄/CO₂) in the H₂O-alkane interface causes a reduction of IFT with rising pressure.^{30,36–38} This is in contrast to the reported pressure effect in two-phase systems of H₂O+alkane, where the IFT typically increases with pressure.^{43,44} Moreover, the IFTs of the CH₄/CO₂-oil interface are barely influenced by the presence of H₂O. Nevertheless, there is no existing information available in the literature on the IFT of the hydrogen+water+oil three-phase mixture.

In this investigation, we carry out the first examination of the interfacial behaviors in the hydrogen+water+normal decane system in three-phase region. To estimate the interfacial properties, we employed extensive MD simulations and density gradient theory (DGT) calculations with the Perturbed-chain Statistical Associating Fluid Theory (PC-SAFT) equation of state (EoS). The results obtained from both methods were compared for a comprehensive analysis. The results from the three-component three-phase mixture are also compared to those from the two-component two-phase mixtures to acquire a deeper understanding of the impacts of the third component.

Moreover, the impacts of temperature and pressure on interfacial properties are investigated. The subsequent sections provide detailed information on the computation and interpretation of IFTs, density profiles, solubilities, enrichments, surface excesses, and spreading coefficients.

2 Method

2.1 Molecular Simulation

All molecular simulations in this work were conducted using the LAMMPS code.⁴⁵ Our simulation system include H₂, H₂O, and n-decane (see Fig.1). The Mie potential is employed to describe the potential energy between segments i and j :⁴⁶

$$U^{\text{Mie}}(r_{ij}) = C_{ij}\varepsilon_{ij} \left[\left(\frac{\sigma_{ij}}{r_{ij}} \right)^{\lambda_{ij}^r} - \left(\frac{\sigma_{ij}}{r_{ij}} \right)^{\lambda_{ij}^a} \right], \quad (1)$$

where r_{ij} denotes the distance between segments, ε_{ij} denotes the well depth, and σ_{ij} denotes the effective segment diameter. The λ_{ij}^a and λ_{ij}^r are the exponents for attractive and repulsive interactions, separately. The following equation is used to compute the constant C :

$$C_{ij} = \left(\frac{\lambda_{ij}^r}{\lambda_{ij}^r - \lambda_{ij}^a} \right) \left(\frac{\lambda_{ij}^r}{\lambda_{ij}^a} \right)^{\lambda_{ij}^a / (\lambda_{ij}^r - \lambda_{ij}^a)}. \quad (2)$$

The fluid components are modeled as coarse-grained (CG) segments. While atomistic models could be devised, CG models not only accurately replicate the experimental interfacial tension,^{47,48} but also significantly decrease the computational expenses. The H₂ and H₂O molecules are described by single CG segments,^{49,50} while the CG model for the n-decane molecule contains three segments connected by two bonds.⁵¹ The bonding energy is described using a harmonic model: $U_{\text{Bond}} = k_{\text{bond}}(r_{\text{ss}} - r_{0,\text{ss}})^2$, where k_{bond} , r_{ss} , and $r_{0,\text{ss}}$ are the spring constant (3333 K/Å²),⁵² distance between bonded segments, and equilibrium bond length (4.4908 Å),⁴⁰ separately. The angle bending

energy is also described using a harmonic model: $U_{\text{Angle}} = k_{\text{angle}}(\theta - \theta_0)^2$, where k_{angle} is the spring constant (1333.54 K/rad⁻²), θ is the angle resulted from the sequential connection of three segments in one molecule, and θ_0 is the equilibrium angle (157.6 °),⁵³ respectively. The non-bonded 1-3 interactions are included.⁵³ The force field parameters for different segments are provided in Tab. 1, Eq. 3, and Eq. 4.

$$(\varepsilon/k_B)/\text{K} = -4.806 \times 10^{-4}(\text{T/K})^2 + 0.6107 \times (\text{T/K}) + 165.9, \quad (3)$$

$$\sigma/\text{nm} = -6.455 \times 10^{-10}(\text{T/K})^3 + 9.100 \times 10^{-7}(\text{T/K})^2 - 4.291 \times 10^{-4}(\text{T/K}) + 0.3543, \quad (4)$$

where T is the temperature in the unit of K. The mixing rules given by Laffitte et al.⁵⁴ are employed to derive the interaction parameters between dissimilar segments:

$$\sigma_{ij} = \frac{\sigma_{ii} + \sigma_{jj}}{2}, \quad (5)$$

$$\varepsilon_{ij} = (1 - k_{ij}) \frac{(\sigma_{ii}^3 \sigma_{jj}^3)^{0.5}}{\sigma_{ij}^3} (\varepsilon_{ii} \varepsilon_{jj})^{0.5}, \quad (6)$$

$$\lambda_{ij}^l = [(\lambda_{ii}^l - 3)(\lambda_{jj}^l - 3)]^{0.5} + 3 \quad l = a, r, \quad (7)$$

where k_{ij} refers the binary interaction parameter. The values of k_{ij} for H₂-H₂O, H₂O-decane segment, and H₂-decane segment pairs are 0.26, 0.28, and 0.0, correspondingly. The non-zero k_{ij} values are tuned based on experimental IFT data of 2-phase fluid mixtures.^{21,22,55,56} A cutoff distance of 20 Å was implemented for the Mie interactions among segments.

Fig. 1 demonstrates equilibrium snapshots of the molecular system for studying the interfacial properties of the H₂+H₂O+decane three-phase mixture. The simulation box boundaries were set to be periodic. The system was made of three cuboid-shaped phases, namely, the H₂-rich phase (connected through the periodic boundary condition), the H₂O-rich phase, and decane-rich phase. There were around 2300 H₂O molecules, 420 decane molecules, and up to 1500 gas molecules. The dimensions of the

simulation box were set to be 44 Å in both the x and y directions. The size of the box in the z direction was approximately 9 times greater than in the other dimensions. These sizes have been tested to be large enough to sufficiently mitigate the size effect in this work and previous studies.⁴² The initial positions of segments were generated using the Packmol code.⁵⁷ The velocity Verlet algorithm was utilized to calculate the particle trajectories.⁵⁸ The timestep used for simulations was 5 fs. The times for the NPT equilibrium and NVT production simulations were 15 ns and 75 ns, respectively. Additionally, temperature and pressure control were separately managed using the Nosé-Hoover thermostat and barostat techniques.

The determination of IFTs follows the Kirkwood and Buff method,⁵⁹ which involves computing the IFT from the pressure tensor components for each interface:

$$\gamma = \int \left[P_{zz} - \frac{1}{2}(P_{xx} + P_{yy}) \right] dz. \quad (8)$$

The pressure tensor components P_{xx} , P_{yy} , and P_{zz} correspond to the diagonal elements. To accurately calculate the spatial distributions of the pressure tensor using the Irving-Kirkwood contour,⁶⁰ we utilized the package developed by Nakamura et al.⁶¹ The results from production simulations were divided into 3 blocks to evaluate uncertainties.

2.2 Density Gradient Theory

The interfacial behaviors of the H₂+water+decane three-phase mixture were also investigated using DGT^{62,63} with PC-SAFT EoS.^{64,65} Details regarding DGT with PC-SAFT EoS can be found in previous studies.^{39,43} Briefly, a three-phase flash calculation was first performed to obtain equilibrium bulk properties which serve as boundary conditions for the DGT.⁶⁶ Subsequently, the DGT was employed for each pair of phases to determine the interfacial properties.⁶⁷ Tabs. S1-S4 provide the parameters utilized in the PC-SAFT DGT. Those parameters were taken either from previous studies^{30,43,64,68-70} or fitted based on experimental data.^{14,21,22,55,71} To validate our models, we compared the IFT results for two-component two-phase systems at various temper-

ature and pressure conditions from both simulation and theory to available experiment data in the literature.^{21,22,55,72} The IFT results obtained from MD, DGT, and experiment exhibit a good agreement as displayed in Figs. S1-S3. Furthermore, reasonable agreement can also be seen between MD and DGT for most of the other bulk or interfacial properties including the component density profiles (Figs. S4-S6), solubilities (Figs. S7-S9), enrichments (Figs. S10-S12), and relative adsorptions (Figs. S13-S15) in the two-phase systems.

3 Results and Discussion

3.1 Interface between hydrogen-rich and water-rich phases

Initially, we investigate the H₂-H₂O interface in the three-phase mixture consisting of H₂, H₂O, and n-decane. Fig. 2 illustrates the IFT values from both MD simulation and DGT for this interface. The simulation predictions align well with the results from DGT, albeit the simulation results are slightly lower than those obtained from DGT. The IFTs values obtained from simulation and theory under the specified temperature and pressure conditions range from 55.0 to 69.6 mN/m and 50.2 to 66.7 mN/m, respectively. It is observed that the IFTs exhibit a decrease as the pressure or temperature increase, which is similar to the trends observed in prior experimental investigations of the H₂+H₂O two-phase system (also see Fig. S1).²¹⁻²⁵ Fig. S16(a) depicts a comparison of IFTs between the H₂+H₂O+decane three-phase mixture and the hydrogen+water two-phase mixture. Generally, the IFTs in the three-phase mixture are lower than those in the two-phase mixture. Additionally, the reductions in IFTs are more pronounced at higher temperatures within the three-phase system. For instance, at 20 MPa, the disparity between the two IFT values computed from DGT rises from 4.9 to 5.3 mN/m when rising the temperature from 298 to 373 K. Nevertheless, when comparing the reduction of IFTs, it is observed that the decreases in IFT values from simulations are mostly less significant compared to results obtained from

the theory, particularly at lower temperatures. Remarkably, a similar reduction trend of IFT of the gas-water interface has been reported in the previous investigations on the $\text{CH}_4+\text{H}_2\text{O}+\text{C}_{10}\text{H}_{22}$ and $\text{CO}_2+\text{H}_2\text{O}+\text{C}_{10}\text{H}_{22}$ three-phase systems.^{38,41}

Due to thermal fluctuations, measuring the density distributions of components within interfacial regions poses a challenge in the experiment.⁷³ However, in MD simulation and DGT, the spatial distributions of each component in the interface are readily accessible.^{39,43,73,74} Fig. 3 illustrates the spatial distributions of hydrogen, water, and $\text{C}_{10}\text{H}_{22}$ obtained from both MD simulations and DGT analysis. The density profiles computed from simulations exhibit consistency with results from the theory. Moreover, the shapes of the density profiles for H_2 and H_2O resemble those observed in the $\text{H}_2+\text{H}_2\text{O}$ two-phase mixture³⁰(see Fig. S4).

The component solubility can be evaluated based on density profiles in the bulk regions. Figs. S17(a,b,d,e) give the solubilities in the H_2O -rich and hydrogen-rich phases of the three-phase mixture. The results are almost the same with solubilities in the two-phase mixtures given in Figs. S7-S9, which indicates the effects of the third component on solubilities are moderate. Notably, the H_2 solubilities in the aqueous phase (Fig. S17a) from simulations are lower than data from the theory, while an opposite behavior is seen for the water solubilities in the hydrogen-rich phase (Fig. S17b). Here, the difference between MD and DGT comes mainly from the CG models used in MD simulations given the force field parameters of H_2O are fitted based mainly on experimental surface tension data.⁵⁰ Furthermore, the solubilities of decane in the aqueous phase from MD simulations given in Fig. S17d are off as expected considering the small absolute value of decane solubility.⁷⁵

As anticipated, the density profile of H_2O shows a continuous decrease from the aqueous phase to the hydrogen-rich phase. Conversely, a distinct peak in the spatial distribution of H_2 in the interfacial region is observed, particularly noticeable at 298 K. Interestingly, the interfacial region also exhibits a maximum density for $\text{C}_{10}\text{H}_{22}$. Moreover, the DGT analysis predicts a greater quantity of $\text{C}_{10}\text{H}_{22}$ within the interfacial region. These density peaks of the oil component within the interfacial regions are as-

sociated with the boundaries of phases and are considered precursors to the emergence of a new phase.^{76,77} These findings align with previous investigations conducted on the 3-phase systems of the $\text{CH}_4+\text{water}+\text{C}_{10}\text{H}_{22}$ and $\text{CO}_2+\text{water}+\text{C}_{10}\text{H}_{22}$ mixtures.^{38,41}

Enrichment is a commonly employed measure to evaluate the non-monotonic behavior of component density profiles:^{78,79}

$$E_i = \frac{\max(n_i(z))}{\max(n_i^I, n_i^{II})}, \quad (9)$$

where $n_i(z)$ represents the spatial distribution of species i across the interface, and n_i^I and n_i^{II} represent the densities of species i in bulk phases I and II , respectively. Fig. 4 presents the enrichments of H_2 and $\text{C}_{10}\text{H}_{22}$ in the $\text{H}_2\text{-H}_2\text{O}$ interface. The enrichments of H_2 decline with pressure and temperature in line with those in the two-phase system (cf. Fig. S10). However, the values in the three-phase mixture are generally smaller than those in the two-phase mixture, especially at low temperature and pressure conditions. The enrichments of $\text{C}_{10}\text{H}_{22}$ also decline with pressure and temperature, while the corresponding values are much larger than those of H_2 .

To comprehend the behaviors of IFT, the surface excess can be examined. The connection between the IFT and the surface excess is determined by the Gibbs adsorption equation:^{73,80–83}

$$-d\gamma = \sum_i \Gamma_{i,j} d\mu_i, \quad (10)$$

where $\Gamma_{i,j}$ denotes the surface excess of species i with the reference species j . The expression for the surface excess is given by:^{84,85}

$$\Gamma_{i,j} = -(n_i^{II} - n_i^I) \int_{-\infty}^{+\infty} \left[\frac{n_j(z) - n_j^{II}}{n_j^{II} - n_j^I} - \frac{n_i(z) - n_i^{II}}{n_i^{II} - n_i^I} \right] dz, \quad (11)$$

where I refers to the phase enriched with component i and II denotes the phase enriched with component j . Fig. 5 presents the surface excesses of H_2 and $\text{C}_{10}\text{H}_{22}$ in the $\text{H}_2\text{-H}_2\text{O}$ interface. The surface excess of H_2 reduces as both pressure and temperature

increase. The same temperature effect can be seen for the surface excess of H_2 in the two-phase system (Fig. S13). However, the surface excess of H_2 in the two-phase system rises first and then declines with rising pressure. The change of pressure effects on H_2 surface excess comes from the presence of decane in the interfacial region which leads to less space for H_2 . The positive values of surface excesses of $\text{C}_{10}\text{H}_{22}$ account for the reduction in IFT after including the $\text{C}_{10}\text{H}_{22}$ into the system based on the analysis of Eq. 10. Moreover, the surface excesses of $\text{C}_{10}\text{H}_{22}$ are pronounced at elevated temperatures consistent with the greater difference of IFT between the two-phase and three-phase systems at higher temperatures.

3.2 Interface between water-rich and decane-rich phases

We then investigate the $\text{H}_2\text{O}-\text{C}_{10}\text{H}_{22}$ interface in the three-phase mixture. Fig. 6 illustrates the values of IFT predicted from both MD simulation and DGT. The simulation data corresponds closely to the predictions made by DGT. The IFTs calculated from MD simulations and the DGT, within the specified conditions, fall within the ranges of 41.9 to 55.0 mN/m and 42.3 to 51.4 mN/m, respectively. It is observed that the IFTs exhibit an increase as the pressure rises or temperature declines. The pressure dependence of IFT is almost linear in the three-phase system. Those findings are similar to the trends observed in prior experimental or simulation investigations of the $\text{H}_2\text{O}+\text{C}_{10}\text{H}_{22}$ two-phase mixture^{43,55} (see Fig. S2). Remarkably, the increments of IFT with pressure from MD simulations are greater than predictions from DGT in the three-phase system, while similar slope is observed in the two-phase mixture (see Fig. S2).

Fig. S16(b) depicts a comparison of IFTs between the $\text{H}_2+\text{H}_2\text{O}+\text{decane}$ three-phase mixture and the $\text{H}_2\text{O}+\text{decane}$ two-phase mixture. Generally, the IFTs in the three-phase mixture are lower than those in the two-phase mixture, especially at elevated pressures. In other words, the linear slope of the IFT-pressure relation declines when H_2 is included in the $\text{H}_2\text{O}-\text{C}_{10}\text{H}_{22}$ interface in contrast to the $\text{H}_2\text{O}-\text{C}_{10}\text{H}_{22}$ two-phase mixture. For example, at 333 K, the linear slopes from the least-square fitting

for two-phase and three-phase systems are 0.0715 (0.0536) mN/(m· MPa) and 0.0447 (0.0079) mN/(m· MPa) from MD (values in parentheses are from DGT), respectively. A similar reduction trend of IFT of the gas-water interface has been reported in the previous investigations on the $\text{CH}_4+\text{H}_2\text{O}+\text{C}_{10}\text{H}_{22}$ and $\text{CO}_2+\text{H}_2\text{O}+\text{C}_{10}\text{H}_{22}$ three-phase systems.^{38,41} However, the reductions of IFT caused by CH_4 and CO_2 are more significant than the H_2 case, and increasing the pressure can even decrease the value of IFT in the water-decane interface of the three-phase mixtures with CH_4 or CO_2 .^{38,41}

Fig. 7 illustrates the spatial distributions for the water- $\text{C}_{10}\text{H}_{22}$ interface. The density distributions computed from MD simulations are in line with the ones from DGT. Moreover, the shapes of the density distributions for H_2O and $\text{C}_{10}\text{H}_{22}$ resemble those observed in the $\text{H}_2\text{O}+\text{C}_{10}\text{H}_{22}$ two-phase mixture⁴³(see Fig. S5). The component solubility can be evaluated based on density profiles in the bulk regions. Figs. S17(c,f) give the solubilities in the decane-rich phase of the three-phase mixture. The results are almost the same with solubilities in the two-phase systems given in Figs. S8 and S9. Notably, the H_2O solubilities in the oil phase (Fig. S17f) from MD are less than values from DGT. The difference between MD and DGT could be mitigated by using an atomistic force field in the MD simulation.⁴¹ The density distributions of H_2O and $\text{C}_{10}\text{H}_{22}$ show a continuous change from the oil-rich phase to the aqueous phase. Notably, there is a distinct peak in the density profile of H_2 in the interfacial region. These findings on density distributions of H_2O , oil, and gas also align with previous investigations conducted on the 3-phase systems of the $\text{CH}_4+\text{water}+\text{decane}$ and $\text{CO}_2+\text{water}+\text{decane}$ mixtures.^{38,41}

The enrichments of H_2 and $\text{C}_{10}\text{H}_{22}$ within the $\text{H}_2\text{O}-\text{C}_{10}\text{H}_{22}$ interface are depicted in Fig. 8. The enrichments of $\text{C}_{10}\text{H}_{22}$ are approximately one, resembling those observed in the two-phase system (cf. Fig. S11). In addition, the enrichment values of H_2 are positive and decline as pressure and temperature rise.

The corresponding surface excesses of H_2 and $\text{C}_{10}\text{H}_{22}$ are illustrated in Fig. 9. The surface excess of H_2 rises with higher pressure and decreases with higher temperatures. On the other hand, the $\text{C}_{10}\text{H}_{22}$ surface excess values are consistently negative compared

to those in the two-phase system (Fig. S14). However, the impact of pressure on the $C_{10}H_{22}$ surface excess differs between the two-phase and three-phase mixtures. In the three-phase mixture, the $C_{10}H_{22}$ surface excess shows a nearly linear decline with pressure, while in the two-phase mixture, it rises with pressure (cf. Fig. S14). Furthermore, the magnitude of this decrease is more pronounced at lower temperatures. This variation in the pressure influences on the $C_{10}H_{22}$ surface excess is caused by the significant adsorption of H_2 in the interface in contrast to $C_{10}H_{22}$. In accordance with Equation (1), the positive values of H_2 surface excess account for the reduction in IFT after adding H_2 into the H_2O - $C_{10}H_{22}$ interface.

3.3 Interface between hydrogen-rich and decane-rich phases

Fig. 10 depicts the IFT values calculated from both molecular simulations and DGT for the H_2 - $C_{10}H_{22}$ interface. The IFT values exhibit a resemblance to those observed in the hydrogen+decane two-phase mixture (cf. Fig. S3). Specifically, the differences in IFT values from the MD simulations are moderate. Moreover, the disparities in IFT values from the DGT method are also minor, considering that the IFT curves for the three-phase mixture and the two-phase mixture overlap with each other, as demonstrated in Fig. S16(c). Fig. 11 illustrates the density distributions of each component within the three-phase systems. Upon comparison with the spatial distributions in the H_2 + $C_{10}H_{22}$ two-phase mixture shown in Fig. S6, only minor differences are noticeable. The densities of H_2O are relatively low in contrast to the densities of the other components. Consequently, the limited influence of H_2O on IFT can be attributed to its low solubility in both the decane-rich phase⁷⁵ and the H_2 -rich phase^{30,86} under relatively high pressure conditions. The enrichments of H_2 in the three-phase systems given in Fig. 12a exhibit nearly identical trends to those observed in the two-phase mixture in Fig. S12. Interestingly, H_2O enrichments are relatively large and decrease as pressure and temperature rise given in Fig. 12b. Additionally, the disparities between the H_2 surface excesses and those of $C_{10}H_{22}$ (the reference species) in the three-phase mixture (Fig. 13a) and the two-phase mixture (Fig. S15) are also negligible. It is worth noting

that H₂O surface excesses displayed in Fig. 13b have positive values, and exhibit an increment with rising temperature.

3.4 Spreading Coefficient

The spreading coefficient, denoted as S , can be employed to determine whether the oil has the ability to form a thin film that spreads between phases.^{87,88} The estimation of S can be accomplished by utilizing the IFTs obtained from the three-phase mixtures:

$$S = \lambda_{wg} - \lambda_{wo} - \lambda_{og}, \quad (12)$$

where λ_{wg} represents the IFT of the water-gas interface, λ_{wo} represents the IFT of the oil-water interface, and λ_{og} represents the IFT of the gas-oil interface of the three-phase mixture. When a positive value of S is obtained, it indicates the ability of the oil film to spread and create a separation between the H₂-rich phase and the H₂O-rich phase. For our simulation system (see Fig. 1), a positive S may lead to the formation of a new oil phase separating the water-rich and gas-rich phases because of the lower interfacial free energy. Conversely, if the value of S is negative, it indicates the formation of an oil droplet.^{89,90}

Fig. 14 displays the values of S in the hydrogen+water+C₁₀H₂₂ 3-phase mixture. It is found that values of S grow with rising pressure and temperature. The values of S obtained from MD are consistent with data predicted by DGT, and fall in ranges from -3.5 to 1.0 mN/m and from -7.4 to -1.5 mN/m for MD and DGT, separately. The values of S from MD are systematically larger than those from DGT because of larger λ_{wg} values (see Fig. 2). The majority of the S values are negative, which suggests the occurrence of oil droplet. At 373 K and around 100 MPa, the S is at around 1.0 mN/m. However, the new oil phase is not observed by checking the density profiles, possibly due to the relatively moderate value of S . In this case, our system corresponds to a metastable three-phase state.

4 Conclusion

This article investigates the interfacial characteristics of the $\text{H}_2+\text{H}_2\text{O}+\text{n-decane}$ three-phase mixture under various temperature (298, 333, and 373 K) and pressure (up to approximately 110 MPa) conditions. To estimate the interfacial properties, both MD simulation and DGT modeling using the PC-SAFT equation of state are employed. Remarkably, these two methods yield consistent estimations, demonstrating good agreement between them. Our findings reveal that IFTs of the gas-water interface in the hydrogen+water+n-decane three-phase mixture are lower compared to IFTs in the hydrogen+water two-phase mixture. This decrease in IFT can be attributed to the excess of the oil component in the interfacial region. In addition, hydrogen accumulates in the interfacial region of the water-oil interface in the three-phase mixture, which weakens the increment of IFT with increasing pressure compared to IFTs in the $\text{H}_2\text{O}+\text{oil}$ two-phase mixture. The IFTs of the hydrogen-oil interface are barely influenced by H_2O due to the limited amount of dissolved H_2O in bulk phases. Nevertheless, relatively strong enrichments and positive surface excesses of water are observed in the hydrogen-oil interfacial region. Moreover, the spreading coefficients predominantly exhibit negative values, which suggests the existence of the three-phase contact for the hydrogen+water+n-decane mixture. This research provides significant insights into the fundamental understanding of interfacial phenomena in the three-phase systems involving hydrogen, water, and oil. These findings can be utilized to enhance the design of processes related to the underground storage of hydrogen in depleted oil fields.

Acknowledgments

This project is supported by the National Natural Science Foundation of China under Grant No. 42203041, the Natural Science Foundation of Jiangsu Province under Grant No. BK20221132, and the China Postdoctoral Science Foundation under Grant No. 2022M723398.

Supporting Information

Additional tables and figures are given in the Supplementary Materials.

References

- (1) Houghton, J. Global warming. *Reports on Progress in Physics* **2005**, *68*, 1343.
- (2) Vicente-Serrano, S. M.; Quiring, S. M.; Pena-Gallardo, M.; Yuan, S.; Dominguez-Castro, F. A review of environmental droughts: Increased risk under global warming? *Earth-Science Reviews* **2020**, *201*, 102953.
- (3) Momirlan, M.; Veziroglu, T. Current status of hydrogen energy. *Renewable and Sustainable Energy Reviews* **2002**, *6*, 141–179.
- (4) Midilli, A.; Ay, M.; Dincer, I.; Rosen, M. A. On hydrogen and hydrogen energy strategies: I: current status and needs. *Renewable and Sustainable Energy Reviews* **2005**, *9*, 255–271.
- (5) Caglayan, D. G.; Weber, N.; Heinrichs, H. U.; Linßen, J.; Robinius, M.; Kukla, P. A.; Stolten, D. Technical potential of salt caverns for hydrogen storage in Europe. *International Journal of Hydrogen Energy* **2020**, *45*, 6793–6805.
- (6) Tarkowski, R. Underground hydrogen storage: Characteristics and prospects. *Renewable and Sustainable Energy Reviews* **2019**, *105*, 86–94.
- (7) Zivar, D.; Kumar, S.; Foroozesh, J. Underground hydrogen storage: A comprehensive review. *International Journal of Hydrogen Energy* **2021**, *46*, 23436–23462.
- (8) Sambo, C.; Dudun, A.; Samuel, S. A.; Esenenjor, P.; Muhammed, N. S.; Haq, B. A review on worldwide underground hydrogen storage operating and potential fields. *International Journal of Hydrogen Energy* **2022**, *47*, 22840–22880.
- (9) Thomas, D. C.; Benson, S. M. *Carbon dioxide capture for storage in deep geologic formations-results from the CO₂ Capture Project: Vol 2-Geologic Storage of Carbon Dioxide with Monitoring and Verification*; Elsevier, 2015.

- (10) Lankof, L.; Tarkowski, R. Assessment of the potential for underground hydrogen storage in bedded salt formation. *International Journal of Hydrogen Energy* **2020**, *45*, 19479–19492.
- (11) Panfilov, M.; Gravier, G.; Fillacier, S. Underground storage of H₂ and H₂-CO₂-CH₄ mixtures. ECMOR X-10th European conference on the mathematics of oil recovery. 2006; pp cp–23.
- (12) Pichler, M. Underground sun storage results and outlook. EAGE/DGMK joint workshop on underground storage of hydrogen. 2019; pp 1–4.
- (13) Tarkowski, R.; Uliasz-Misiak, B.; Tarkowski, P. Storage of hydrogen, natural gas, and carbon dioxide—Geological and legal conditions. *International Journal of Hydrogen Energy* **2021**, *46*, 20010–20022.
- (14) Florusse, L.; Peters, C.; Pàmies, J.; Vega, L. F.; Meijer, H. Solubility of hydrogen in heavy n-alkanes: Experiments and saft modeling. *AIChE Journal* **2003**, *49*, 3260–3269.
- (15) Yellig, W.; Metcalfe, R. Determination and Prediction of CO₂ Minimum Miscibility Pressures. *Journal of Petroleum Technology* **1980**, *32*, 160–168.
- (16) Rao, D. N.; Lee, J. I. Determination of gas–oil miscibility conditions by interfacial tension measurements. *Journal of Colloid and Interface Science* **2003**, *262*, 474–482.
- (17) Hosseini, M.; Fahimpour, J.; Ali, M.; Keshavarz, A.; Iglauer, S. Capillary sealing efficiency analysis of caprocks: implication for hydrogen geological storage. *Energy & Fuels* **2022**, *36*, 4065–4075.
- (18) Yekta, A.; Manceau, J.-C.; Gaboreau, S.; Pichavant, M.; Audigane, P. Determination of hydrogen–water relative permeability and capillary pressure in sandstone: application to underground hydrogen injection in sedimentary formations. *Transport in Porous Media* **2018**, *122*, 333–356.

- (19) Pan, B.; Yin, X.; Ju, Y.; Iglauer, S. Underground hydrogen storage: Influencing parameters and future outlook. *Advances in Colloid and Interface Science* **2021**, *294*, 102473.
- (20) Luboń, K.; Tarkowski, R. Influence of capillary threshold pressure and injection well location on the dynamic CO₂ and H₂ storage capacity for the deep geological structure. *International Journal of Hydrogen Energy* **2021**, *46*, 30048–30060.
- (21) Chow, Y. F.; Maitland, G. C.; Trusler, J. M. Interfacial tensions of (H₂O+H₂) and (H₂O+CO₂+H₂) systems at temperatures of (298–448) K and pressures up to 45 MPa. *Fluid Phase Equilibria* **2018**, *475*, 37–44.
- (22) Chow, Y. F.; Maitland, G. C.; Trusler, J. M. Erratum to Interfacial tensions of (H₂O+H₂) and (H₂O+CO₂+H₂) systems at temperatures of (298 to 448) K and pressures up to 45 MPa[Fluid Phase Equil. 475 (2018) 37–44]. **2020**,
- (23) Hosseini, M.; Fahimpour, J.; Ali, M.; Keshavarz, A.; Iglauer, S. H₂-brine interfacial tension as a function of salinity, temperature, and pressure; implications for hydrogen geo-storage. *Journal of Petroleum Science and Engineering* **2022**, *213*, 110441.
- (24) Slowinski Jr, E. J.; Gates, E. E.; Waring, C. E. The effect of pressure on the surface tensions of liquids. *The Journal of Physical Chemistry* **1957**, *61*, 808–810.
- (25) Massoudi, R.; King Jr, A. Effect of pressure on the surface tension of water. Adsorption of low molecular weight gases on water at 25. deg. *The Journal of Physical Chemistry* **1974**, *78*, 2262–2266.
- (26) Isfehiani, Z. D.; Sheidaie, A.; Hosseini, M.; Fahimpour, J.; Iglauer, S.; Keshavarz, A. Interfacial tensions of (brine+H₂+CO₂) systems at gas geo-storage conditions. *Journal of Molecular Liquids* **2023**, *374*, 121279.

- (27) Muhammed, N. S.; Haq, B.; Al Shehri, D. A. Hydrogen storage in depleted gas reservoirs using nitrogen cushion gas: A contact angle and surface tension study. *International Journal of Hydrogen Energy* **2023**,
- (28) Mirchi, V.; Dejam, M.; Alvarado, V. Interfacial tension and contact angle measurements for hydrogen-methane mixtures/brine/oil-wet rocks at reservoir conditions. *International Journal of Hydrogen Energy* **2022**, *47*, 34963–34975.
- (29) van Rooijen, W.; Habibi, P.; Xu, K.; Dey, P.; Vlugt, T.; Hajibeygi, H.; Moulton, O. Interfacial tensions, solubilities, and transport properties of the H₂/H₂O/NaCl system: A molecular simulation study. *Journal of Chemical & Engineering Data* **2023**,
- (30) Yang, Y.; Nair, A. K. N.; Zhu, W.; Sang, S.; Sun, S. Molecular Perspectives of Interfacial Properties of the Hydrogen+Water Mixture in Contact with Silica or Kerogen. *Journal of Molecular Liquids* **2023**, 122337.
- (31) Doan, Q. T.; Keshavarz, A.; Miranda, C. R.; Behrenbruch, P.; Iglauer, S. Molecular dynamics simulation of interfacial tension of the CO₂-CH₄-water and H₂-CH₄-water systems at the temperature of 300 K and 323 K and pressure up to 70 MPa. *Journal of Energy Storage* **2023**, *66*, 107470.
- (32) Bahramian, A.; Danesh, A.; Gozalpour, F.; Tohidi, B.; Todd, A. Vapour-liquid interfacial tension of water and hydrocarbon mixture at high pressure and high temperature conditions. *Fluid Phase Equilibria* **2007**, *252*, 66–73.
- (33) Pereira, L., et al. Interfacial tension of reservoir fluids: an integrated experimental and modelling investigation. Ph.D. thesis, Heriot-Watt University, 2016.
- (34) Pereira, L. M. C.; Chapoy, A.; Tohidi, B., et al. Vapor-liquid and liquid-liquid interfacial tension of water and hydrocarbon systems at representative reservoir conditions: Experimental and modelling results. SPE Annual Technical Conference and Exhibition. 2014.

- (35) Amin, R.; Smith, T. N. Interfacial tension and spreading coefficient under reservoir conditions. *Fluid Phase Equilibria* **1998**, *142*, 231–241.
- (36) Pan, Z.; Trusler, J. M. Experimental and modelling study of the interfacial tension of (n-decane+carbon dioxide+water) in the three phase region. *Fluid Phase Equilibria* **2023**, *568*, 113760.
- (37) Yang, D.; Tontiwachwuthikul, P.; Gu, Y. Interfacial tensions of the crude oil+reservoir brine+CO₂ systems at pressures up to 31 MPa and temperatures of 27 C and 58 C. *Journal of Chemical & Engineering Data* **2005**, *50*, 1242–1249.
- (38) Yang, Y.; Ruslan, M. F. A. C.; Sun, S. Study of interfacial properties of water+methane+oil three-phase systems by a simple molecular simulation protocol. *Journal of Molecular Liquids* **2022**, *356*, 118951.
- (39) Yang, Y.; Zhu, W.; Ji, Y.; Wang, T.; Zhao, G. Interfacial properties of H₂O+CO₂+oil three-phase systems: a density gradient theory study. *Atmosphere* **2022**, *13*, 625.
- (40) Lobanova, O.; Mejia, A.; Jackson, G.; Mueller, E. A. SAFT- γ force field for the simulation of molecular fluids 6: Binary and ternary mixtures comprising water, carbon dioxide, and n-alkanes. *The Journal of Chemical Thermodynamics* **2016**, *93*, 320–336.
- (41) Yang, Y.; Ruslan, M. F. A. C.; Zhu, W.; Zhao, G.; Sun, S. Interfacial behaviors of the H₂O+CO₂+CH₄+C₁₀H₂₂ system in three phase equilibrium: A combined molecular dynamics simulation and density gradient theory investigation. *Journal of Molecular Liquids* **2023**, *370*, 121031.
- (42) Yang, Y.; Narayanan Nair, A. K.; Sun, S. Molecular dynamics simulation study of carbon dioxide, methane, and their mixture in the presence of brine. *The Journal of Physical Chemistry B* **2017**, *121*, 9688–9698.

- (43) Yang, Y.; Narayanan Nair, A. K.; Anwari Che Ruslan, M. F.; Sun, S. Bulk and interfacial properties of the decane+water system in the presence of methane, carbon dioxide, and their mixture. *The Journal of Physical Chemistry B* **2020**, *124*, 9556–9569.
- (44) Yang, Y.; Nair, A. K. N.; Ruslan, M. F. A. C.; Sun, S. Interfacial properties of the alkane+water system in the presence of carbon dioxide and hydrophobic silica. *Fuel* **2022**, *310*, 122332.
- (45) Plimpton, S. Fast parallel algorithms for short-range molecular dynamics. *Journal of Computational Physics* **1995**, *117*, 1–19.
- (46) Mie, G. Zur kinetischen Theorie der einatomigen Körper. *Annalen der Physik* **1903**, *316*, 657–697.
- (47) Miguez, J. M.; Garrido, J. M.; Blas, F. J.; Segura, H.; Mejia, A.; Pineiro, M. M. Comprehensive characterization of interfacial behavior for the mixture CO₂+H₂O+CH₄: Comparison between atomistic and coarse grained molecular simulation models and density gradient theory. *The Journal of Physical Chemistry C* **2014**, *118*, 24504–24519.
- (48) Garrido, J. M.; Quinteros-Lama, H.; Miguez, J. M.; Blas, F. J.; Pineiro, M. M. On the physical insight into the barotropic effect in the interfacial behavior for the H₂O+CO₂ mixture. *The Journal of Physical Chemistry C* **2019**, *123*, 28123–28130.
- (49) Hirshfelder, J. O.; Curtiss, C. F.; Bird, R. B. Molecular Theory of Gases and Liquids. *New York* **1954**,
- (50) Lobanova, O.; Avendano, C.; Lafitte, T.; Müller, E. A.; Jackson, G. SAFT- γ force field for the simulation of molecular fluids: 4. A single-site coarse-grained model of water applicable over a wide temperature range. *Molecular Physics* **2015**, *113*, 1228–1249.

- (51) Herdes, C.; Totton, T. S.; Müller, E. A. Coarse grained force field for the molecular simulation of natural gases and condensates. *Fluid Phase Equilibria* **2015**, *406*, 91–100.
- (52) Rahman, S.; Lobanova, O.; Jiménez-Serratos, G.; Braga, C.; Raptis, V.; Muller, E. A.; Jackson, G.; Avendano, C.; Galindo, A. SAFT- γ Force Field for the simulation of molecular fluids. 5. Hetero-group coarse-grained models of linear alkanes and the importance of intramolecular interactions. *The Journal of Physical Chemistry B* **2018**, *122*, 9161–9177.
- (53) Herdes, C.; Petit, C.; Mejía, A.; Muller, E. A. Combined experimental, theoretical, and molecular simulation approach for the description of the fluid-phase behavior of hydrocarbon mixtures within shale rocks. *Energy & Fuels* **2018**, *32*, 5750–5762.
- (54) Lafitte, T.; Apostolakou, A.; Avendaño, C.; Galindo, A.; Adjiman, C. S.; Müller, E. A.; Jackson, G. Accurate statistical associating fluid theory for chain molecules formed from Mie segments. *The Journal of Chemical Physics* **2013**, *139*, 154504.
- (55) Georgiadis, A.; Maitland, G.; Trusler, J. M.; Bismarck, A. Interfacial tension measurements of the (H₂O+n-decane+CO₂) ternary system at elevated pressures and temperatures. *Journal of Chemical & Engineering Data* **2011**, *56*, 4900–4908.
- (56) Cai, B.-Y.; Yang, J.-T.; Guo, T.-M. Interfacial tension of hydrocarbon+water/brine systems under high pressure. *Journal of Chemical & Engineering Data* **1996**, *41*, 493–496.
- (57) Martínez, L.; Andrade, R.; Birgin, E. G.; Martínez, J. M. PACKMOL: A package for building initial configurations for molecular dynamics simulations. *Journal of Computational Chemistry* **2009**, *30*, 2157–2164.

- (58) Frenkel, D.; Smit, B. *Understanding molecular simulation: from algorithms to applications*; Elsevier, 2001; Vol. 1.
- (59) Kirkwood, J. G.; Buff, F. P. The statistical mechanical theory of surface tension. *The Journal of Chemical Physics* **1949**, *17*, 338–343.
- (60) Irving, J.; Kirkwood, J. G. The statistical mechanical theory of transport processes. IV. The equations of hydrodynamics. *The Journal of Chemical Physics* **1950**, *18*, 817–829.
- (61) Nakamura, T.; Kawamoto, S.; Shinoda, W. Precise calculation of the local pressure tensor in Cartesian and spherical coordinates in LAMMPS. *Computer Physics Communications* **2015**, *190*, 120–128.
- (62) Davis, H.; Scriven, L. Stress and structure in fluid interfaces. *Advances in Chemical Physics* **1982**, *49*, 357–454.
- (63) Van der Waals, J. Thermodynamische Theorie der Kapillarität unter voraussetzung stetiger Dichteänderung. *Zeitschrift für Physikalische Chemie* **1894**, *13*, 657–725.
- (64) Gross, J.; Sadowski, G. Perturbed-chain SAFT: An equation of state based on a perturbation theory for chain molecules. *Industrial & Engineering Chemistry Research* **2001**, *40*, 1244–1260.
- (65) Gross, J.; Sadowski, G. Application of the perturbed-chain SAFT equation of state to associating systems. *Industrial & Engineering Chemistry Research* **2002**, *41*, 5510–5515.
- (66) Pan, H.; Connolly, M.; Tchelep, H. Multiphase equilibrium calculation framework for compositional simulation of CO₂ injection in low-temperature reservoirs. *Industrial & Engineering Chemistry Research* **2019**, *58*, 2052–2070.

- (67) Mejía, A.; Müller, E. A.; Chaparro Maldonado, G. SGTPy: A Python Code for Calculating the Interfacial Properties of Fluids Based on the Square Gradient Theory Using the SAFT-VR Mie Equation of State. *Journal of Chemical Information and Modeling* **2021**, *61*, 1244–1250.
- (68) Alanazi, A.; Ali, M.; Bawazeer, S.; Yekeen, N.; Hoteit, H. Evaluation of cubic, PC-SAFT, and GERG2008 equations of state for accurate calculations of thermophysical properties of hydrogen-blend mixtures. *Energy Reports* **2022**, *8*, 13876–13899.
- (69) Diamantonis, N. I.; Economou, I. G. Evaluation of statistical associating fluid theory (SAFT) and perturbed chain-SAFT equations of state for the calculation of thermodynamic derivative properties of fluids related to carbon capture and sequestration. *Energy & Fuels* **2011**, *25*, 3334–3343.
- (70) Mairhofer, J.; Gross, J. Modeling properties of the one-dimensional vapor-liquid interface: Application of classical density functional and density gradient theory. *Fluid Phase Equilibria* **2018**, *458*, 243–252.
- (71) Alvarez, J.; Fernández-Prini, R. A semiempirical procedure to describe the thermodynamics of dissolution of non-polar gases in water. *Fluid Phase Equilibria* **1991**, *66*, 309–326.
- (72) Linstrom, P. J.; Mallard, W. G. The NIST Chemistry WebBook: A chemical data resource on the internet. *Journal of Chemical & Engineering Data* **2001**, *46*, 1059–1063.
- (73) Stephan, S.; Hasse, H. Enrichment at vapour–liquid interfaces of mixtures: Establishing a link between nanoscopic and macroscopic properties. *International Reviews in Physical Chemistry* **2020**, *39*, 319–349.
- (74) Yang, Y.; Che Ruslan, M. f. A.; Narayanan Nair, A. K.; Qiao, R.; Sun, S. Inter-

- facial properties of the hexane+carbon dioxide+water system in the presence of hydrophilic silica. *The Journal of Chemical Physics* **2022**,
- (75) Maczyński, A.; Wiśniewska-Gocłowska, B.; Góral, M. Recommended liquid–liquid equilibrium data. Part 1. Binary alkane–water systems. *Journal of Physical and Chemical Reference Data* **2004**, *33*, 549–577.
- (76) Falls, A.; Scriven, L.; Davis, H. Adsorption, structure, and stress in binary interfaces. *The Journal of Chemical Physics* **1983**, *78*, 7300–7317.
- (77) Stephan, S.; Hasse, H. Interfacial properties of binary mixtures of simple fluids and their relation to the phase diagram. *Physical Chemistry Chemical Physics* **2020**, *22*, 12544–12564.
- (78) Becker, S.; Werth, S.; Horsch, M.; Langenbach, K.; Hasse, H. Interfacial tension and adsorption in the binary system ethanol and carbon dioxide: Experiments, molecular simulation and density gradient theory. *Fluid Phase Equilibria* **2016**, *427*, 476–487.
- (79) Stephan, S.; Cárdenas, H.; Mejía, A.; Müller, E. A. The monotonicity behavior of density profiles at vapor–liquid interfaces of mixtures. *Fluid Phase Equilibria* **2023**, *564*, 113596.
- (80) Radke, C. Gibbs adsorption equation for planar fluid–fluid interfaces: Invariant formalism. *Advances in Colloid and Interface Science* **2015**, *222*, 600–614.
- (81) Miqueu, C.; Miguez, J. M.; Pineiro, M. M.; Lafitte, T.; Mendiboure, B. Simultaneous application of the gradient theory and Monte Carlo molecular simulation for the investigation of methane/water interfacial properties. *The Journal of Physical Chemistry B* **2011**, *115*, 9618–9625.
- (82) Yang, Y.; Che Ruslan, M. F. A.; Narayanan Nair, A. K.; Sun, S. Effect of ion valency on the properties of the carbon dioxide–methane–brine system. *The Journal of Physical Chemistry B* **2019**, *123*, 2719–2727.

- (83) Yang, Y.; Nair, A. K. N.; Ruslan, M. F. A. C.; Sun, S. Interfacial properties of the aromatic hydrocarbon+water system in the presence of hydrophilic silica. *Journal of Molecular Liquids* **2022**, *346*, 118272.
- (84) Telo da Gama, M.; Evans, R. The structure and surface tension of the liquid-vapour interface near the upper critical end point of a binary mixture of Lennard-Jones fluids: I. The two phase region. *Molecular Physics* **1983**, *48*, 229–250.
- (85) Wadewitz, T.; Winkelmann, J. Density functional theory: Structure and interfacial properties of binary mixtures. *Berichte der Bunsengesellschaft für physikalische Chemie* **1996**, *100*, 1825–1832.
- (86) Eller, J.; Sauerborn, T.; Becker, B.; Buntic, I.; Gross, J.; Helmig, R. Modeling Subsurface Hydrogen Storage With Transport Properties From Entropy Scaling Using the PC-SAFT Equation of State. *Water Resources Research* **2022**, *58*, e2021WR030885.
- (87) Shaw, D. J. *Introduction to colloid and surface chemistry*; Butterworths, 1980.
- (88) Harkins, W. D.; Feldman, A. Films. The spreading of liquids and the spreading coefficient. *Journal of the American Chemical Society* **1922**, *44*, 2665–2685.
- (89) Bonn, D.; Eggers, J.; Indekeu, J.; Meunier, J.; Rolley, E. Wetting and spreading. *Reviews of Modern Physics* **2009**, *81*, 739.
- (90) Bertrand, E.; Bonn, D.; Meunier, J.; Segal, D. Wetting of alkanes on water. *Physical Review Letters* **2001**, *86*, 3208.

Table 1: Mie force field parameters of different fluid components.

Segment	ε_{ii}/k_B (K)	σ_{ii} (nm)	λ_{ii}^r	λ_{ii}^a	Reference
H ₂	33.3133	0.29700	12.0	6.0	⁴⁹
H ₂ O	Eq. 3	Eq. 4	8.0	6.0	⁵⁰
C ₁₀ H ₂₂	415.1900	0.45841	20.9	6.0	⁵¹

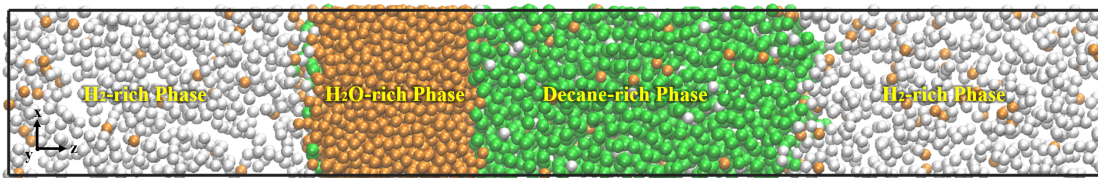


Figure 1: Equilibrium snapshots of the $\text{H}_2+\text{H}_2\text{O}+\text{n-decane}$ three-phase system at 333 K and 20 MPa. Color code: H_2 , white; H_2O , orange; n-decane segment, green.

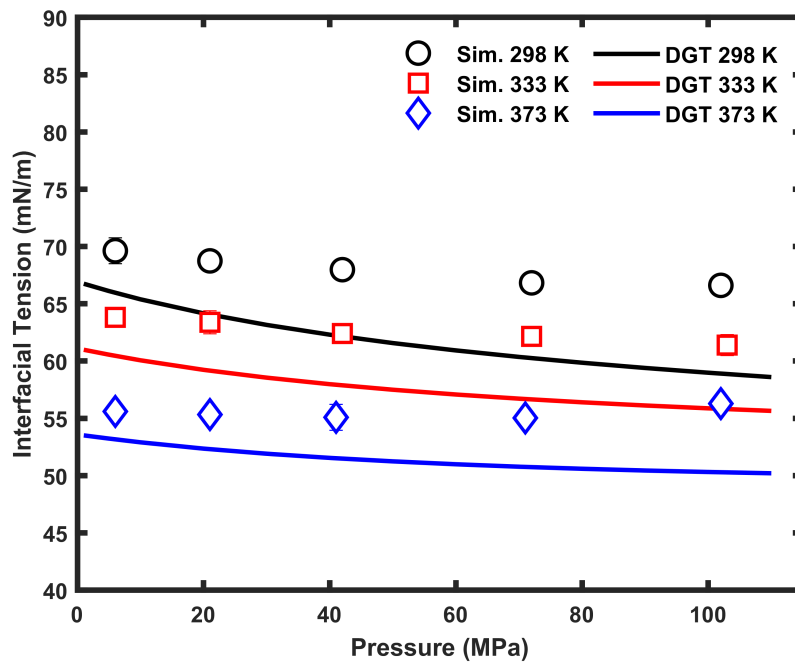


Figure 2: Interfacial tensions as a function of pressure in the $\text{H}_2+\text{H}_2\text{O}+\text{C}_{10}\text{H}_{22}$ 3-phase system for the interface between H_2O -rich phase and H_2 -rich phase. The open symbols represent the data from the MD simulation, and the data obtained using DGT with the PC-SAFT EoS are shown as lines. Error bars smaller than the symbol size are not displayed.

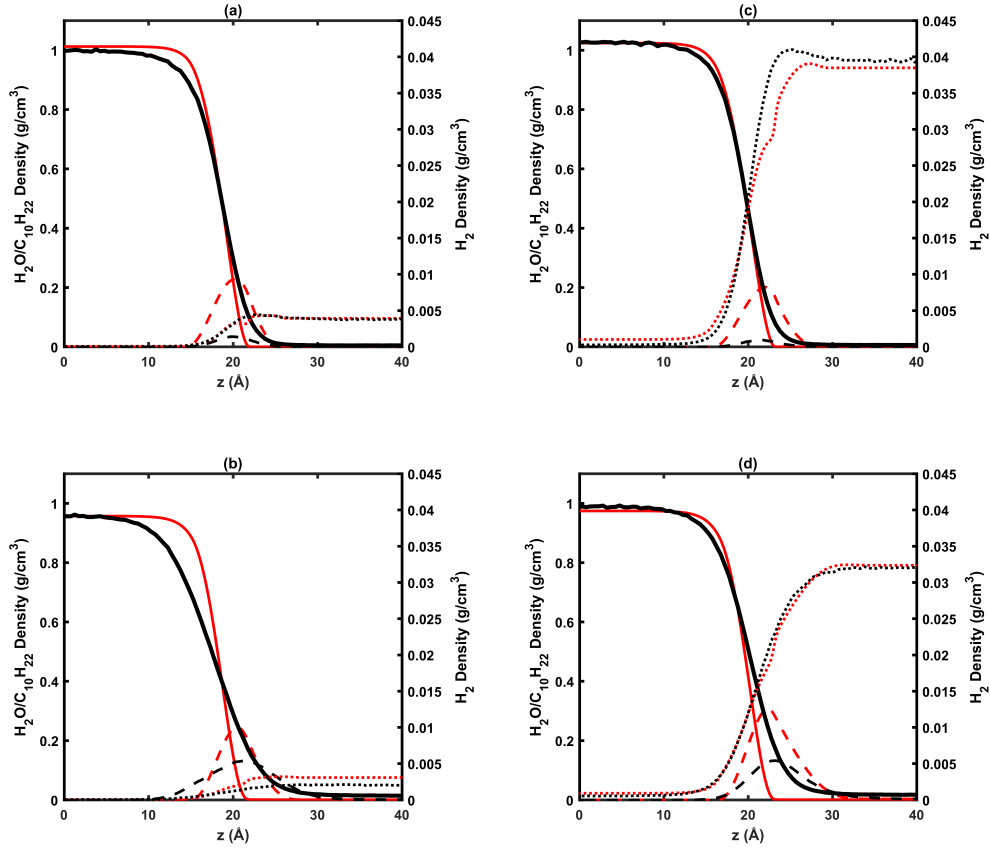


Figure 3: Equilibrium distributions of different species in the $\text{H}_2+\text{H}_2\text{O}+\text{C}_{10}\text{H}_{22}$ 3-phase system for the interface between H_2O -rich phase and vapor phase at (a) 298 K, 5 MPa, (b) 373 K, 5 MPa, (c) 298 K, 70 MPa, and (d) 373 K, 70 MPa. The black and red colors denote MD and DGT data, respectively. The solid, dotted, and dashed lines represent H_2O , H_2 , and $\text{C}_{10}\text{H}_{22}$, respectively.

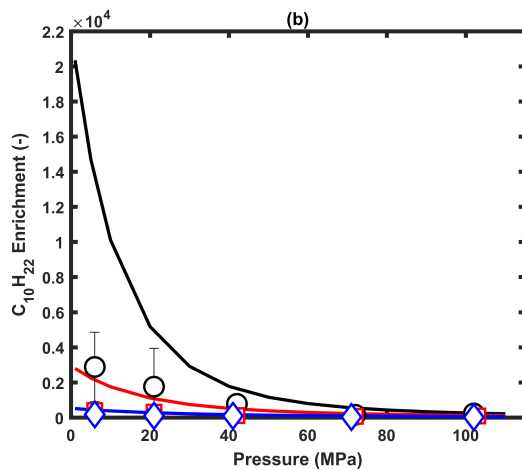
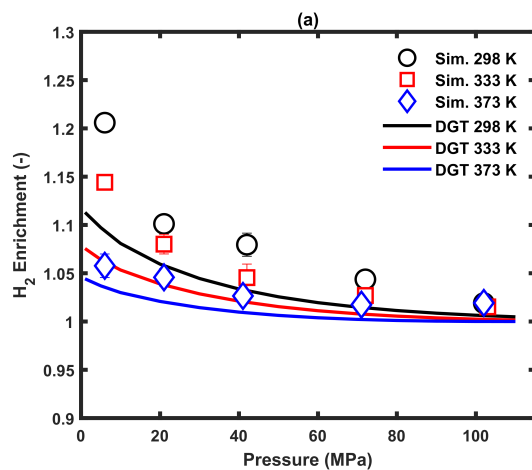


Figure 4: Pressure dependence of component enrichment for the interface between H₂-rich phase and H₂O-rich phase in the H₂+H₂O+C₁₀H₂₂ 3-phase system. The open symbols represent the data from the MD simulation, and the data from DGT with the PC-SAFT EoS are shown as lines.

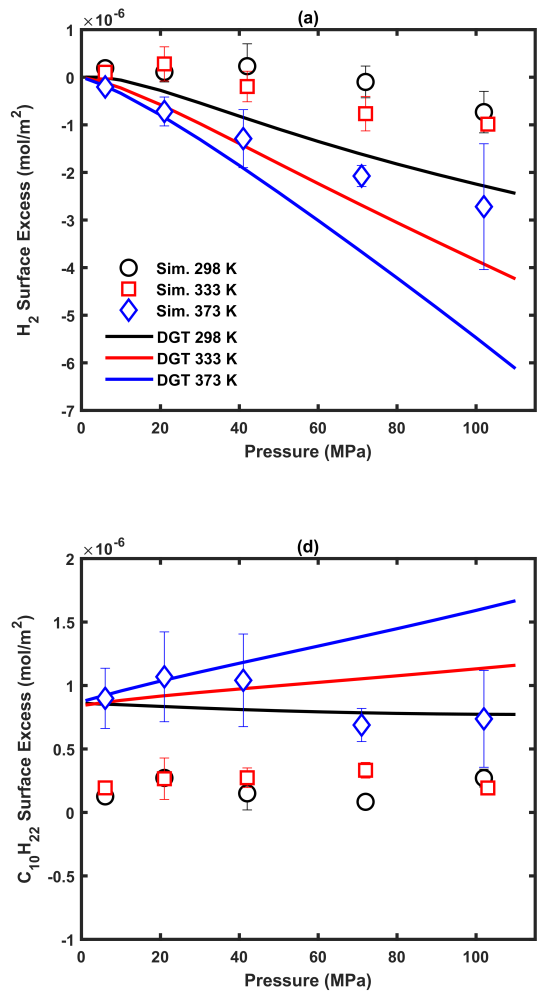


Figure 5: Pressure dependence of component surface excess for the interface between H₂-rich phase and H₂O-rich phase in the H₂+H₂O+C₁₀H₂₂ 3-phase system. The open symbols represent the data from the MD simulation, and the data from DGT with the PC-SAFT EoS are shown as lines.

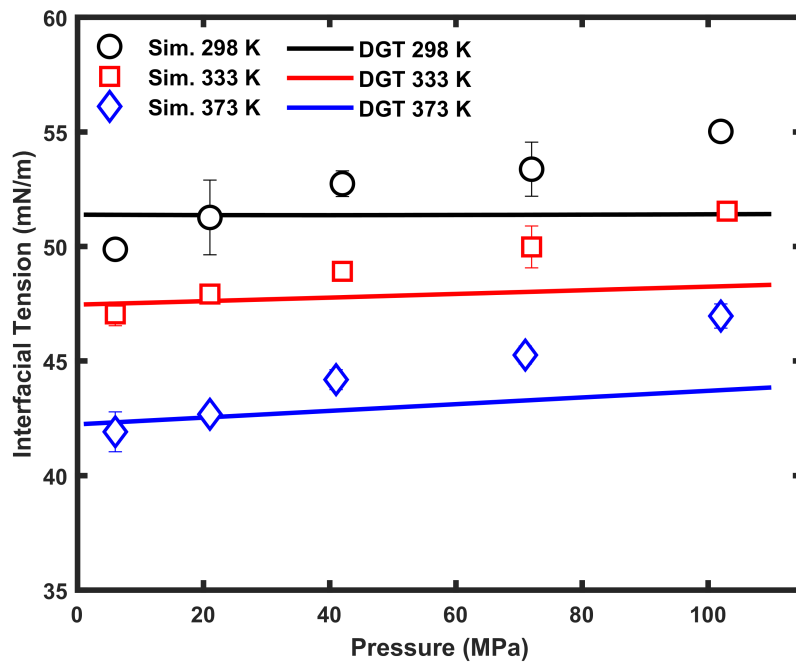


Figure 6: Interfacial tensions as a function of pressure in the $\text{H}_2+\text{H}_2\text{O}+\text{C}_{10}\text{H}_{22}$ 3-phase system for the interface between H_2O -rich phase and $\text{C}_{10}\text{H}_{22}$ -rich phase. The open symbols represent the data from the MD simulation, and the data obtained using DGT with the PC-SAFT EoS are shown as lines. Error bars smaller than the symbol size are not displayed.

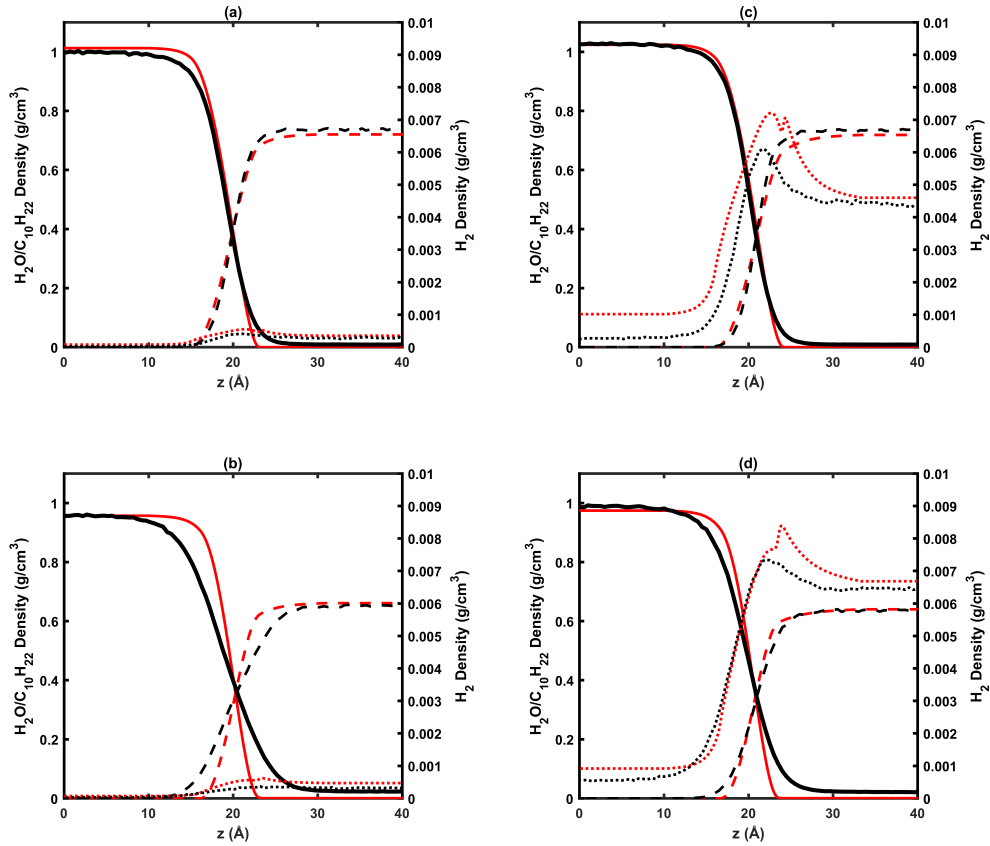


Figure 7: Equilibrium distributions of different species in the $\text{H}_2+\text{H}_2\text{O}+\text{C}_{10}\text{H}_{22}$ 3-phase system for the interface between H_2O -rich phase and $\text{C}_{10}\text{H}_{22}$ -rich phase at (a) 298 K, 5 MPa, (b) 373 K, 5 MPa, (c) 298 K, 70 MPa, and (d) 373 K, 70 MPa. The black and red colors denote MD and DGT data, respectively. The solid, dotted, and dashed lines represent H_2O , H_2 , and $\text{C}_{10}\text{H}_{22}$, respectively

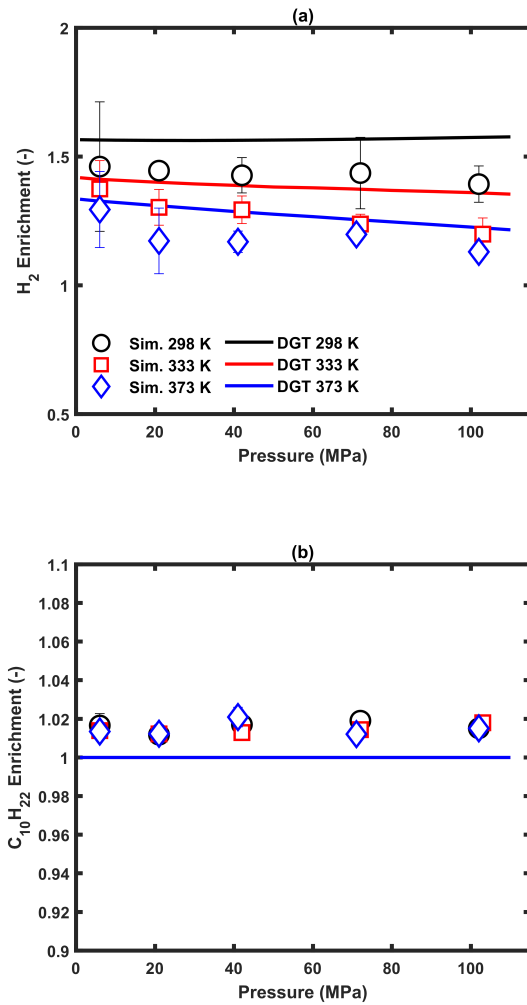


Figure 8: Pressure dependence of component enrichment for the interface between H₂O-rich phase and C₁₀H₂₂-rich phase in the H₂+H₂O+C₁₀H₂₂ 3-phase system. The open symbols represent the data from the MD simulation, and the data from DGT with the PC-SAFT EoS are shown as lines.

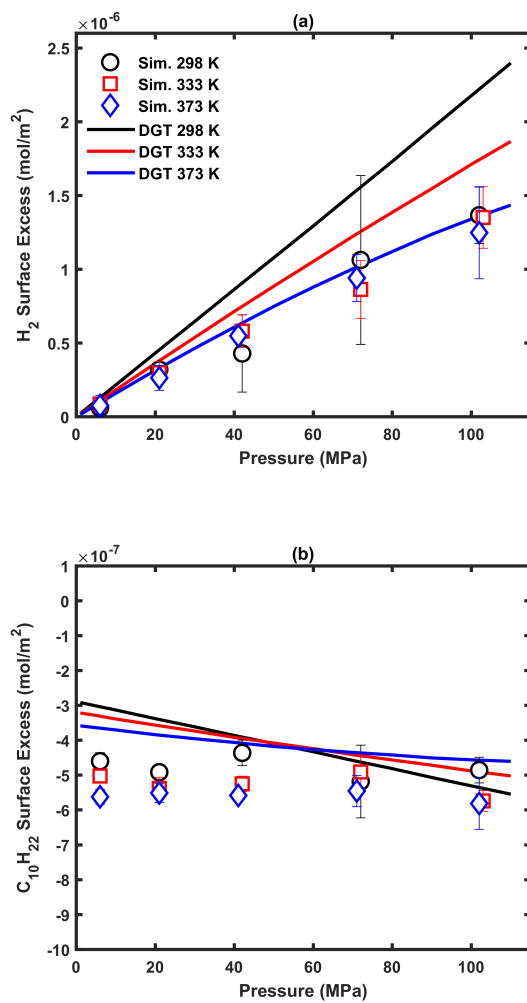


Figure 9: Pressure dependence of component surface excess for the interface between H₂O-rich phase and C₁₀H₂₂-rich phase in the H₂+H₂O+C₁₀H₂₂ 3-phase system. The open symbols represent the data from the MD simulation, and the data from DGT with the PC-SAFT EoS are shown as lines.

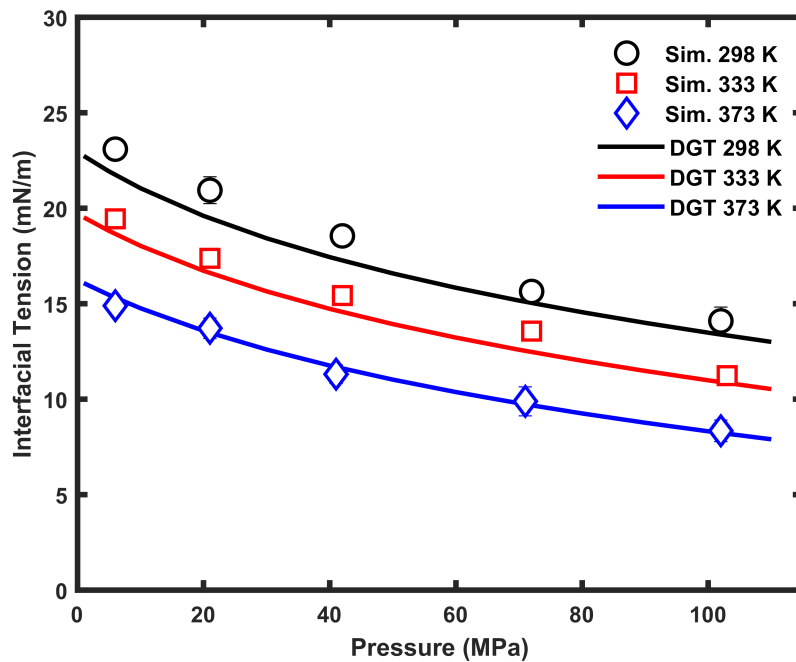


Figure 10: Interfacial tensions as a function of pressure in the $\text{H}_2+\text{H}_2\text{O}+\text{C}_{10}\text{H}_{22}$ 3-phase system for the interface between H_2 -rich phase and $\text{C}_{10}\text{H}_{22}$ -rich phase. The open symbols represent the data from the MD simulation, and the data obtained using DGT with the PC-SAFT EoS are shown as lines. Error bars smaller than the symbol size are not displayed.

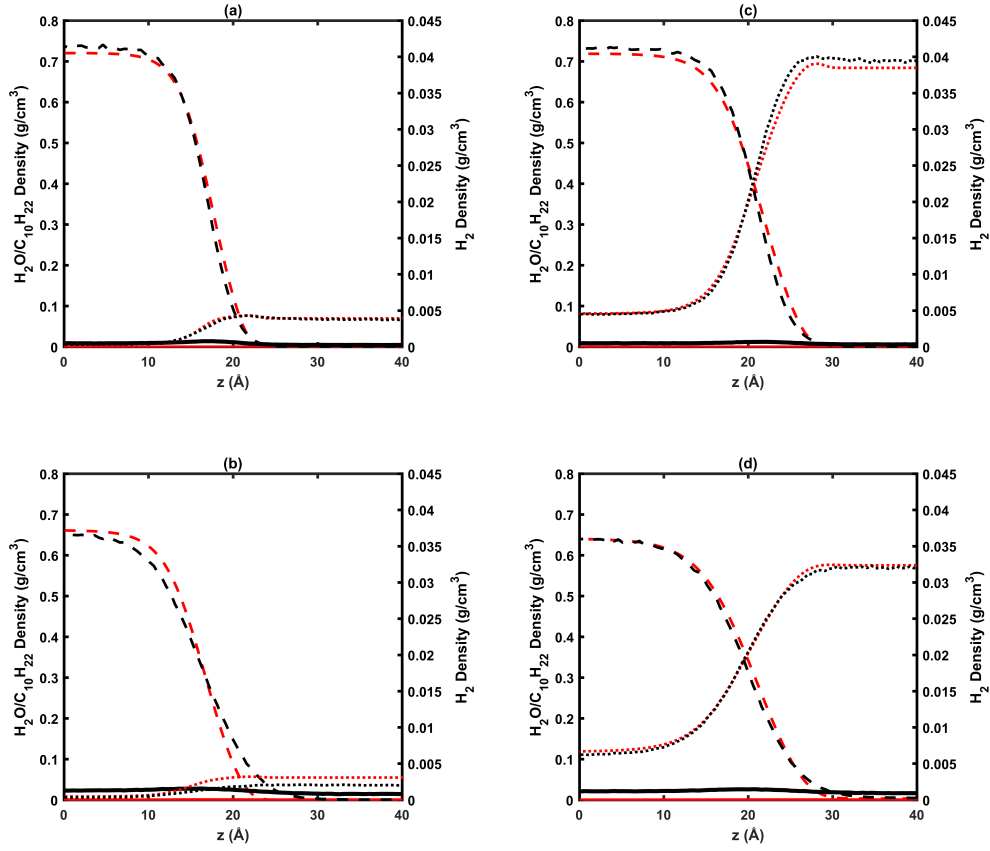


Figure 11: Equilibrium distributions of different species in the $\text{H}_2+\text{H}_2\text{O}+\text{C}_{10}\text{H}_{22}$ 3-phase system for the interface between H_2 -rich phase and $\text{C}_{10}\text{H}_{22}$ -rich phase at (a) 298 K, 5 MPa, (b) 373 K, 5 MPa, (c) 298 K, 70 MPa, and (d) 373 K, 70 MPa. The black and red colors denote MD and DGT data, respectively. The solid, dotted, and dashed lines represent H_2O , H_2 , and $\text{C}_{10}\text{H}_{22}$, respectively

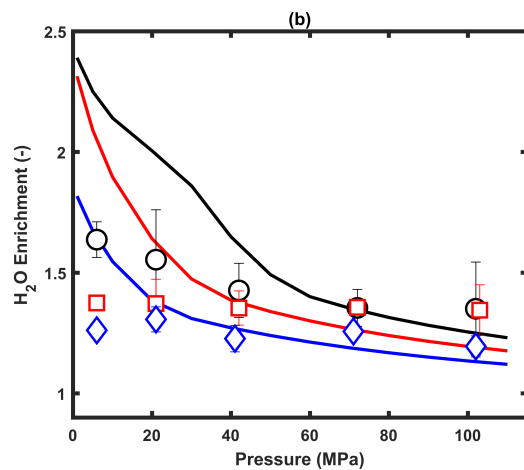
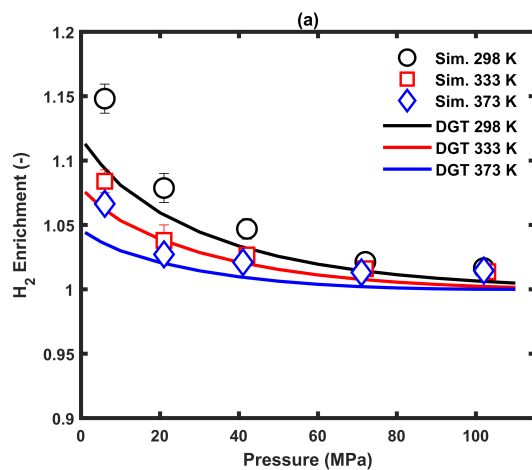


Figure 12: Pressure dependence of component enrichment for the interface between H₂-rich phase and C₁₀H₂₂-rich phase in the H₂+H₂O+C₁₀H₂₂ 3-phase system. The open symbols represent the data from the MD simulation, and the data from DGT with the PC-SAFT EoS are shown as lines.

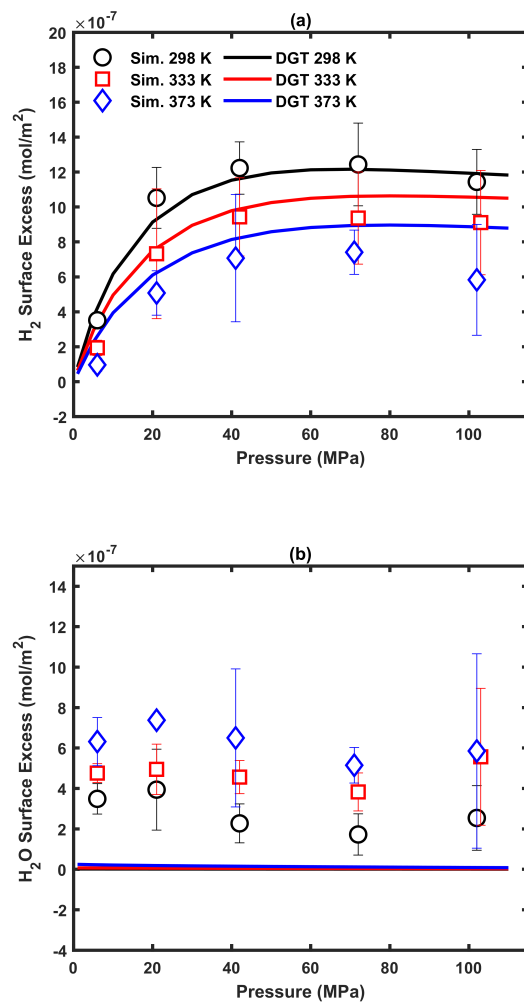


Figure 13: Pressure dependence of component surface excess for the interface between H₂-rich phase and C₁₀H₂₂-rich phase in the H₂+H₂O+C₁₀H₂₂ 3-phase system. The open symbols represent the data from the MD simulation, and the data from DGT with the PC-SAFT EoS are shown as lines.

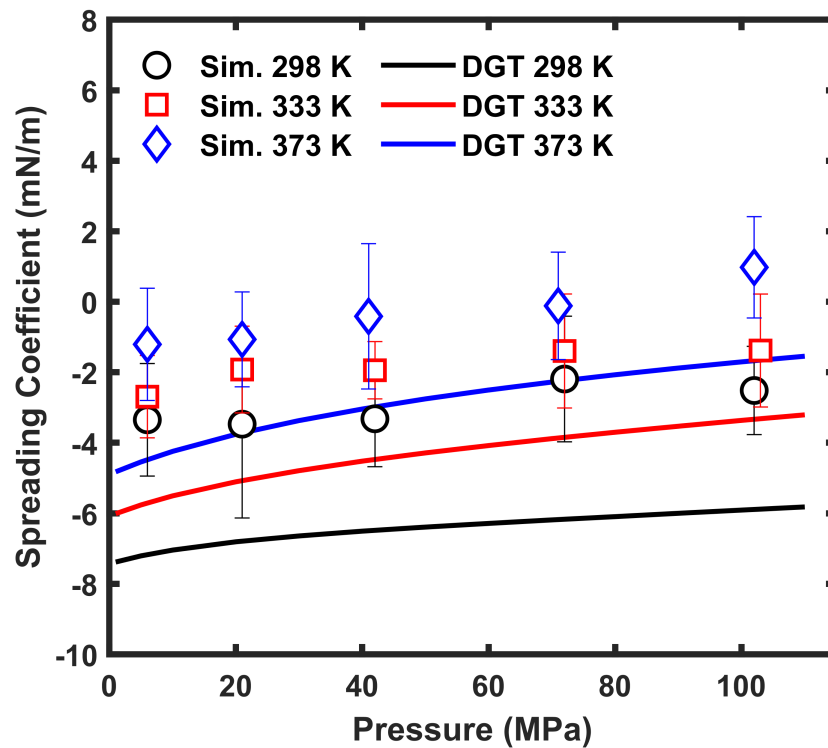
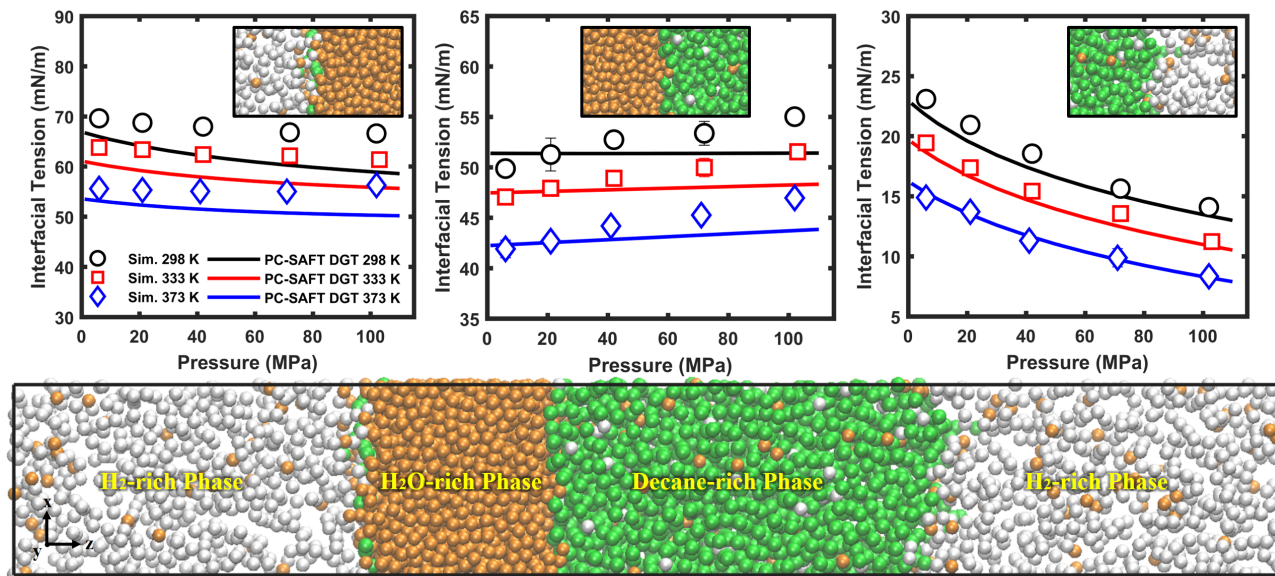


Figure 14: Spreading coefficient as a function of pressure in the $\text{H}_2+\text{H}_2\text{O}+\text{C}_{10}\text{H}_{22}$ 3-phase system. The open symbols represent the results from the MD simulation, and the estimates obtained using DGT with the PC-SAFT EoS are shown as lines.



TOC Graphic